Effective Separation Method for Single-Channel Time-Frequency Overlapped Signals Based on Improved Empirical Wavelet Transform

Zhipeng Liu[1*], Lichun Li[1], Huiqi Li[1], and Chang Liu[2]

[1] National Digital System Engineering and Technological Research R&D Center
Zhengzhou, 450001 - China
[e-mail: liuzhip1994@163.com]
[2] School of Resources Environment and Chemical Engineering of Nanchang University
Nanchang, 330031 - China
[e-mail: 18720991215@163.com]
*Corresponding author: Zhipeng Liu

Abstract

To improve the separation performance of time-frequency overlapped radar and communication signals from a single channel, this paper proposes an effective separation method based on an improved empirical wavelet transform (EWT) that introduces a fast boundary detection mechanism. The fast boundary detection mechanism can be regarded as a process of searching, difference optimization, and continuity detection of the important local minima in the Fourier spectrum that enables determination of the sub-band boundary and thus allows multiple signal components to be distinguished. An orthogonal empirical wavelet filter bank that was designed for signal adaptive reconstruction is then used to separate the input time-frequency overlapped signals. The experimental results show that if two source components are completely overlapped within the time domain and the spectrum overlap ratio is less than 60%, the average separation performance is improved by approximately 32.3% when compared with the classic EWT; the proposed method also improves the suitability for multiple frequency shift keying (MFSK) and reduces the algorithm complexity.

1. Introduction

In modern electronic warfare, multiple input multiple output (MIMO) radar or communication system has become an important tool for electronic reconnaissance and intelligence transmission. As a common MIMO radar or communication signal, different types of modulation modes usually have a serious overlap of both time and frequency in the receivers, and the frequency bands of radar and communication system are generally covered by each other, so it cannot be directly used in the latter signal classification and recognition tasks [1-2].

In non-cooperative reception scenarios, the reconnaissance system often receives hybrid time-frequency overlapped signals, so blind source separation (BSS) is applied to separate the sources from the observations without a priori knowledge on hybrid procedure and the sources [3]. In practical applications, the number of source signals usually exceeds the number of sensors, and such a scenario constitutes underdetermined blind source separation (UBSS) [4]. The most difficult case in UBSS is that there is only one sensors, and it is called single-channel blind source separation (SBSS) [5]. When less information is available, SBSS has no definite mathematical solution; but if enough differences exist between each of the sources, the problem can be solved [6-10].

Empirical mode decomposition (EMD) is used to decompose a signal as a finite sum of intrinsic mode functions (IMFs) and has gained considerable interest for signal analysis applications over the last decade [11-13]. EMD can perform well in the separation of stationary or nonstationary hybrid signals which are completely overlapped within the time domain by using its adaptivity on different time scales, but it is only effective for high sparsity of the source signals in the frequency domain [14-16]. For improving the separation performance for the mixed sources having more serious overlap of frequency, Gilles proposed the empirical wavelet transform (EWT) to extract more information from the frequency domain with reference to EMD [17-18]. EWT usually consists of two steps: segment the Fourier spectrum of hybrid signal into multiple sub band first and then reconstruct the sources. Based on the scale space algorithm, the input hybrid signals were divided into multiple frequency features by determining valid Fourier boundaries, and an orthogonal wavelet filter bank was then designed for signal adaptive construction. However, this method cannot divide MFSK signals correctly and the algorithm's complexity increases sharply with increasing numbers of the sources [19].

Therefore, with the aim of improving the expansibility of the classic EWT, this paper proposes an effective method based on an improved EWT that introduces a new adaptive spectrum division mechanism to improve the separation performance for time-frequency overlapped signals, and particularly for MFSK. In addition, the proposed method also overcomes the problem that causes the algorithm's complexity to rise so sharply.

The rest of this paper is organized as follows. In Sect. 2, we propose three time-frequency overlapped signal models and the basic theory of analysis in the separation problem. Our method and the classic EWT are described in Sect. 3. Section 4 shows the experimental results and analysis. Finally, some conclusions are given in Sect. 5.

2. Related Work

First, the instantaneous linear hybrid SBSS mathematical model with noise, can be represented as:

$$f(t) = [a_1 \ a_2 \ \cdots \ a_n] \begin{bmatrix} s_1(t) \\ s_2(t) \\ \vdots \\ s_n(t) \end{bmatrix} + v(t) = \mathbf{A}\mathbf{s}(t) + v(t) \quad t=1,2,\cdots T \tag{1}$$

where $f(t)$ represents the observed signal, $\mathbf{A} \in R^{1 \times n}$ is the observation matrix, $\mathbf{s}(t)$ represents n source signals, and $v(t)$ is the additive noise.

Seven typical radar and communication signals have been selected as source signal components for study. We chose two types of communication signals (quaternary frequency shift keying (4FSK) and binary phase shift keying (BPSK)) and five types of radar signals (Frank, Barker, even quadratic frequency modulation (EQFM), linear frequency modulation (LFM), and sinusoidal frequency modulation (SFM) signals).

To enable visual representation of the time-frequency characteristics, the Choi-Williams distribution, which is a Cohen class distribution with high time-frequency resolution and fewer cross terms than traditional time-frequency (T-F) distributions [20-21], is used here to analyze the selected signals. Figure 1 shows the time-frequency distribution images for the chosen signal types, where the horizontal axis represents the time and the vertical axis represents the frequency. The images in **Fig. 1** show that large differences exist between the time-frequency distributions of the selected signal types. Therefore, based on their pattern features, the seven signal types can be divided into two distinct classes: stretch-class distributions and compact-class distributions. The LFM, SFM, and EQFM distributions are assumed to be specific curves, represented by stretched shapes, and their frequency bandwidths are relatively wide when compared with those of the other signals; thus they are stretch-class distributions. The distributions of the 4FSK, BPSK, Frank, and Barker signals are more concentrated and have much narrower frequency bandwidths, meaning that they are compact-class distributions. For these stretch and compact-class distribution signals, three models are established for discussion in this paper: the stretch overlapping model, the stretch-compact overlapping model, and the compact overlapping model.
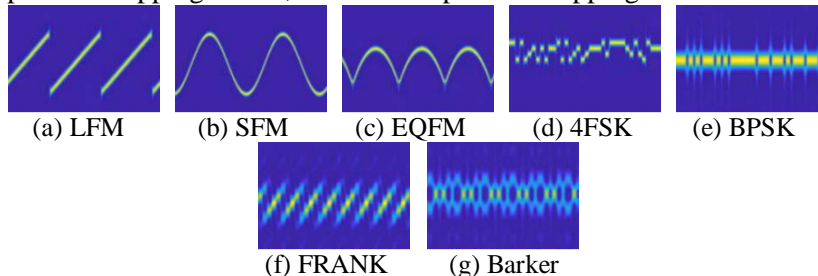

(a) LFM   (b) SFM   (c) EQFM   (d) 4FSK   (e) BPSK

(f) FRANK   (g) Barker

Fig. 1. In this figure, (a)–(g) are different signal types, which including Linear frequency modulation(LFM), Sinusoidal frequency modulation (SFM), Even quadratic frequency modulation (EQFM), quaternary frequency shift keying (4FSK), Binary phase shift keying (BPSK), Frank and Barker sequentially. There are significant differences among the Choi‑Williams time-frequency distribution (CWD) images. The controllable factor $\sigma = 1$ also be used and SNR= 5dB.

In the above models, the necessary assumptions need to be mentioned. On one hand, any two sources of the hybrid signal overlap completely in the time domain. On the other hand, for simplification, it is assumed that the hybrid signal for studying in this paper contains only two sources. Therefore, the overlapping behavior in the frequency domain must be analyzed. The spectrum overlap ratio of the different sources is defined as:

$$\eta_{s_i} = \frac{Bdoverlap_{s_i}}{Bd_{si}} \tag{2}$$

where $Bdoverlap_{s_i}$ represents the overlap bandwidth of source signal s_i that overlaps with the other sources in the Fourier spectrum, and Bd_{s_i} is the entire bandwidth corresponding to s_i .

2.1 Stretch and stretch-compact overlapping models

The stretch overlapping model contains two different types of stretch-class distribution. As shown in **Fig. 2**a, because the time-frequency patterns of the sources are shown as curves, the overlap in the image is indicated by multiple intersection points. In the stretch-compact overlapping model, because of the time-frequency distribution and the more serious nature of the overlapping, more intersection points are generated, as shown in **Fig. 2**b.

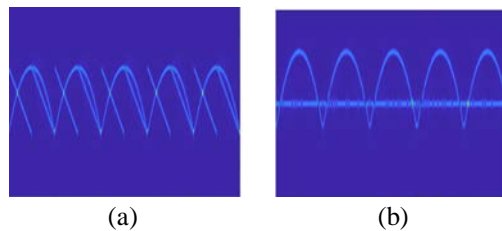(a)   (b)

Fig. 2. (a) The time-frequency sample images of the stretch overlapping model (LFM+EQFM); (b) The time-frequency sample images of stretch-compact overlapping model (EQFM+BPSK).

In these two models, if the spectrum overlap ratio of the source with the narrower bandwidth is 100%, it is fairly easy to recognize the signals from the time-frequency images visually.

2.2 Compact overlapping model

In the compact overlapping model, compact-class distributions have different overlap of frequency. Here, the following five spectrum overlap ratios are set for analysis: 20%, 40%, 60%, 80% and 100%. **Fig. 3** shows the results for Frank and 4FSK signals of the same bandwidth for these different ratios.
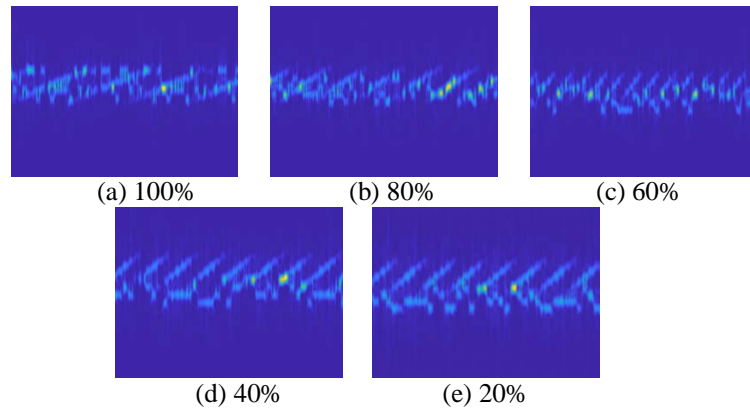
Fig. 3. The time-frequency sample images of the compact overlapping model at different spectrum overlap ratio (FRANK+4FSK, (a) 100%; (b) 80%; (c) 60%; (d) 40%; (e) 20%).

As the spectrum overlap ratio increases, the recognition of each source also becomes more difficult from the vison, and the separation difficulty may be greatly enhanced. When the ratio exceeds 60%, it basically becomes impossible to distinguish the main features of each source from the time-frequency image.

With regard to the multi-component time-frequency overlapped signals that may occur in an actual scene, these signals can be simplified by being decomposed into the three time-frequency overlapped signal models, but these models are only applicable under specific and limited conditions, to ensure good discrimination of each source in the Fourier spectrum, which can be summarized as follows:

Constraint 1. Different frequency bands or modulation modes of adjacent overlapped sources is needed, to ensure that the hybrid signals have good separability.

Constraint 2. A single overlap area can contain two sources at most, which need to meet the constraint 1, but one source signal can contain multiple overlapping areas (no more than two), as shown in **Fig. 4**.

When the two constraints above are satisfied simultaneously, the multi-component time-frequency overlapped signals can then be simplified for analysis using the proposed models.
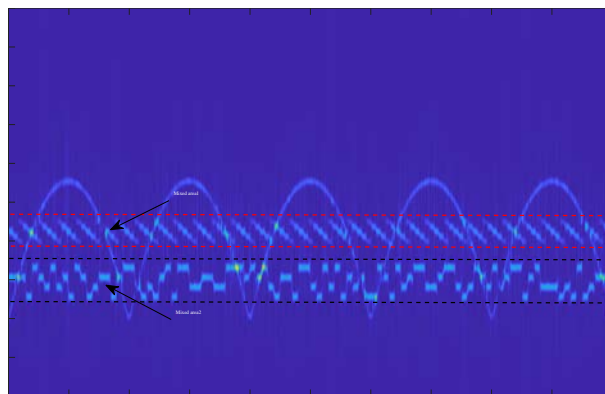

Fig. 4. The sample images of multi-component time-frequency overlapped signal.

3. Improved EWT

3.1 Classic EWT

The classic EWT performs division on the Fourier spectrum by using the scale space algorithm, and then constructs a set of self-adaptive band-pass filters to extract the different signal amplitude-frequency (AF) components from each sub band to achieve separation of the sources [18]. The adaptability of the EWT is mainly reflected in the fact that the parameters of each filter are determined depending upon different sub bands. In the classic EWT, the scale space algorithm is used to determine valid Fourier boundaries by searching and filtering the local maxima in the Fourier spectrum, and the spectrum waveform is quite demanding. The scale space algorithm adopt a time-varying Gaussian kernel to observes both the whole and parts of the spectrum using multiple space scales to obtain one or more "important maxima", where most of these "important maxima" are significantly larger than the other local maxima that exist around them and are thus more representative of the spectrum. Let $\left\{M_k\right\}_{k=1}^{m}$ represents the set of m detected "important maxima". Without any loss of generality, we assumed that this set is sorted in descending order $(M_1 \geq M_2 \geq \cdots M_m)$ and normalized in [0; 1]. To keep the "important maxima" which are greater than some amount of the difference between the bigger maximum and the smaller maximum, we set the threshold $M_m + \beta(M_1 - M_m)$, where β is applied for adjusting the amplitude, generally β =0.3 or 0.4 can be used to achieve a good separation effect [18]. Next, we define the center between the corresponding frequencies of the adjacent M_k as the boundary of each sub band, as shown in **Fig. 5**a. However, this division approach can easily cause severe damage to the spectral integrity of partial sources. This means that the signal may be divided into multiple sub bands, as shown in **Fig. 5**b, and this operation also affects the detection of the weaker signals.
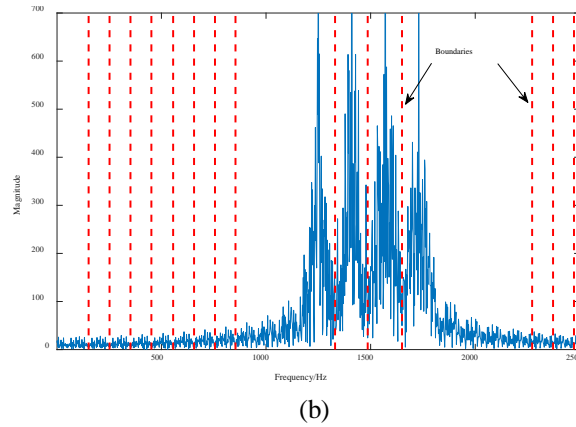

(a)

(b)
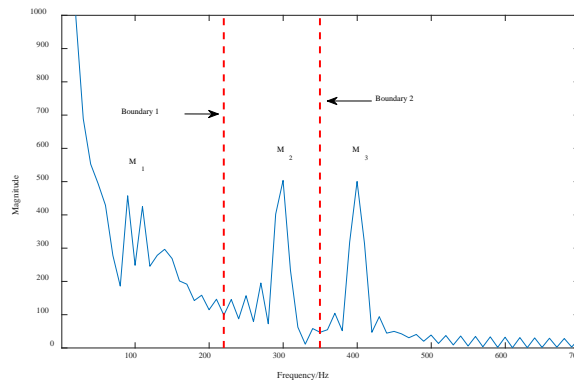
Fig. 5. Boundary detection in classic EWT. (a). Sub-band boundary determination; (b). The division of the spectrum of 4FSK.

3.2 Improved EWT

The core idea of the improved EWT is to use a fast boundary detection mechanism for the Fourier spectrum segmentation procedure. Since the local maxima generally represent the main spectrum features, it is common to lead the neglect of some important but weak signal features, so the local minima in the spectrum are more suitable for detection of the edges of the spectral waveforms of the different sources. The fast boundary detection mechanism mainly uses searching, difference optimization, and continuity detection processes to filter out the important local minima and then determines the sub-band boundaries. The purpose of the new division approach is to produce a stable and efficient algorithm for detection of the sub-band boundaries and then enhance the separation performance for the time-frequency overlapped signals while reducing the algorithm's complexity. Using time-domain discrete signals as an example, the detailed implementation steps for the improved EWT are described as follows:

Step 1: Calculate the Fourier spectrum $F(\omega)$ of the input time-frequency overlapped signal $f(n)$, and the sampling frequency is Fs.

Step 2: Consider a normalized Fourier axis which has a 2π periodicity, in order to respect the Shannon criteria, we restrict the discussion in $[0, \pi]$. Let us start by assuming that the Fourier spectrum $[0, \pi]$ is divided into N contiguous sub band. Each sub band is expressed as $\Lambda_i = [\omega_i, \omega_{i+1}]$, and it is easy to see that $\bigcup_{i=1}^{N} \Lambda_i = [0, \pi]$, where $\omega_1 = 0$ and $\omega_{N+1} = \pi$. The remaining N-1 boundaries are determined by the fast boundary detection mechanism (we will discuss the details of this detection mechanism and how it work later), denoted as $\{\omega_i\}_{i=2}^{N}$.

Step 3: To reconstruct the corresponding sources of each sub band, we construct a set of band pass filters on each Λ_i by utilizing the idea used in the construction of both Littlewood-Paley and Meyer's wavelets [22]. The empirical scaling function and the empirical wavelets are defined as $\hat{\phi}_n(\omega)$ and $\hat{\psi}_n(\omega)$, expressed as (3) and (4), respectively.

$$\hat{\phi}_n(\omega) = \begin{cases} 1 & |\omega| \le (1-\gamma)\omega_n \\ \cos\left[\frac{\pi}{2}\beta\left(\frac{1}{2\gamma\omega_n}(|\omega|-(1-\gamma)\omega_n)\right)\right] & (1-\gamma)\omega_n \le |\omega| \le (1+\gamma)\omega_n \\ 0 & otherwise \end{cases} \quad (3)$$

$$\hat{\psi}_n(\omega) = \begin{cases} 1 & (1+\gamma)\omega_n \le |\omega| \le (1-\gamma)\omega_{n+1} \\ \cos\left[\frac{\pi}{2}\beta\left(\frac{1}{2\gamma\omega_{n+1}}(|\omega|-(1-\gamma)\omega_{n+1})\right)\right] & (1-\gamma)\omega_{n+1} \le |\omega| \le (1+\gamma)\omega_{n+1} \\ \sin\left[\frac{\pi}{2}\beta\left(\frac{1}{2\gamma\omega_n}(|\omega|-(1-\gamma)\omega_n)\right)\right] & (1-\gamma)\omega_n \le |\omega| \le (1+\gamma)\omega_n \\ 0 & otherwise \end{cases} \quad (4)$$

where the function $\beta(x)$ is an arbitrary $C^k([0,1])$ function, and the most used in [22] is expressed as (5). Concerning the choice of γ, we set the value for a tight frame used in [18] as (6).

$$\beta(x) = \begin{cases} 0 & x \le 0 \\ x^4(35-84x+70x^2-20x^3) & \forall x \in [0,1] \\ 1 & x \ge 1 \end{cases} \quad (5)$$

$$\gamma < \min_n\left(\frac{\omega_{n+1}-\omega_n}{\omega_{n+1}+\omega_n}\right) \quad (6)$$

Step 4: From the previous steps, we know how to build a suitable frame set of empirical wavelets. Now we can calculate EWT, in the same way as for the classic wavelet transform. The detail coefficients and approximation coefficients are defined $W_f^\varepsilon(n,t)$ and $W_f^\varepsilon(0,t)$ respectively, expressed as (7) and (8)

$$W_f^\varepsilon(n,t) = \langle f, \psi_n \rangle = \int f(\tau)\overline{\psi}_n(\tau-t)d\tau = F^{-1}(\hat{f}(\omega)\overline{\hat{\psi}}_n(\omega)) \quad (7)$$

$$W_f^\varepsilon(0,t) = \langle f, f_1 \rangle = \int f(\tau)\overline{\phi}_1(\tau-t)d\tau = F^{-1}(\hat{f}(\omega)\overline{\hat{\phi}}_1(\omega)) \quad (8)$$

where f represents the hybrid signal, $\overline{\psi}_n$ is the complex conjugation of ψ_n, $\hat{f}(\omega)$, $\hat{\psi}_n(\omega)$ and $\hat{\phi}_1(\omega)$ are the Fourier transform of $f(t)$, $\psi_n(t)$ and $\phi_1(t)$ respectively, defined by (3) and (4).

Step 5: The reconstruction of the hybrid signal $f(t)$ is represented as (9).

$$f(t) = W_f^\varepsilon(0,t)\phi_1(t) + \sum_{n=1}^{N} W_f^\varepsilon(n,t)\psi_n(t)$$

$$= F^{-1}\left(\hat{W}_f^\varepsilon(0,\omega)\hat{\phi}_1(\omega) + \sum_{n=1}^{N} \hat{W}_f^\varepsilon(n,\omega)\hat{\psi}_n(\omega) \right) \tag{9}$$

where $\hat{W}_f^\varepsilon(0,\omega)$ and $\hat{W}_f^\varepsilon(n,\omega)$ are the Fourier transform of $W_f^\varepsilon(0,t)$ and $W_f^\varepsilon(n,t)$ defined by (7) and (8), respectively. Since $f(t)$ can also be expressed as:

$$f(t) = \sum_{k=0}^{N-1} f_k(t) \tag{10}$$

where $f_k(t)$ is obtained by the decomposition of $f(t)$, it means that the source signals are obtained after the division and reconstruction, defined as (11).

$$\begin{cases} f_0(t) = W_f^\varepsilon(0,t)\phi_1(t) \\ f_k(t) = W_f^\varepsilon(k,t)\psi_k(t) \end{cases} \tag{11}$$

3.3 Fast Boundary Detection Mechanism

We propose a simple and effective method to determine the boundaries between the different sources. First, we search for all local minima within the magnitude of the Fourier spectrum of the input hybrid signal $f(t)$, and let $Min = \{\min_k\}_{k=1}^{m}$ denote the set of m detected minima (where $\{\min_k\}_{k=1}^{m}$ are arranged in ascending order of the corresponding frequency points). In general, we think that the $\min_k$ with smaller values mostly appear between the waveforms of adjacent signals or within the noise spectrum, while the $\min_k$ with larger values usually appear inside the waveforms of the signals. For the latter continuity detection, we define a "local minimum group" comprising consecutive $\min_k$, and the number of $\min_k$ in each local minimum group is set as K, where K is required to be much smaller than the number of all minima m, usually, $K \leq 0.1m$. As shown in **Fig. 6**, regardless of whether an overlap area exists between the sources or not (we use 4FSK+Frank under different spectrum overlap ratios, 0 and 40%), the distribution of the local minimum group located within the noise spectrum is smooth, while slight fluctuations are generated between the adjacent signals. Inside the signals, however, much larger fluctuations are existed. Here the curve *LMcurve* is used to indicate the distribution of $\{\min_k\}_{k=1}^{m}$ uniformly.
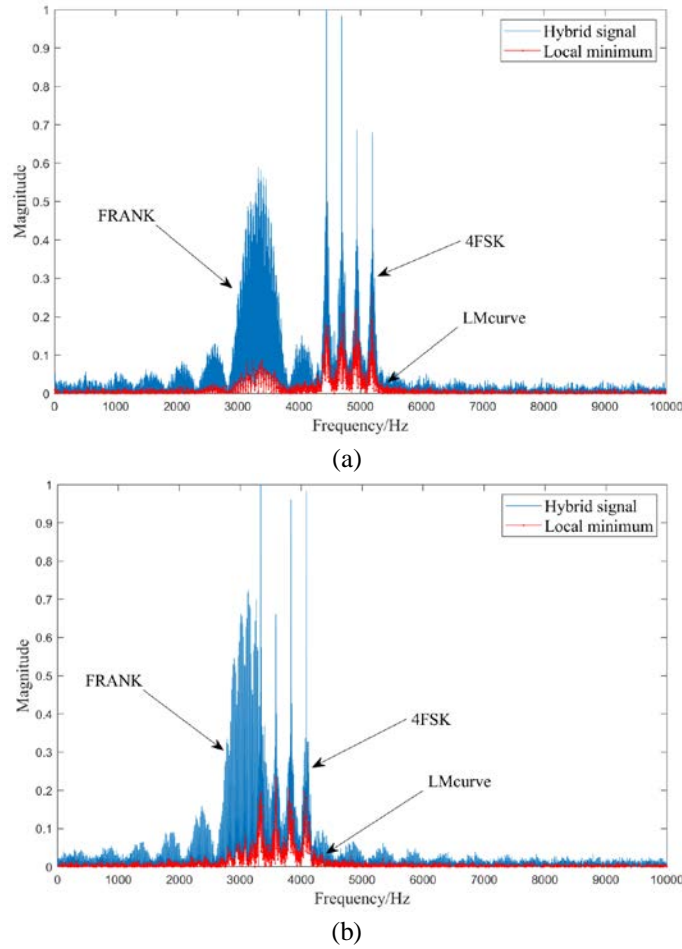
(a)

(b)

Fig. 6. The distribution of local minimum in the Fourier spectrum of input hybrid signal
(4FSK+FRANK). (a) $\eta_{s_1} = \eta_{s_2} = 0$; (b) $\eta_{s_1} = \eta_{s_2} = 40\%$.

To provide a better understanding of the fluctuations, an analysis of the fluctuations in the differences is performed. The difference between the adjacent points is given by:

$$d_k = \min_{k+1} - \min_k \quad k = 1, 2, \cdots m - 1 \tag{12}$$

where d_k represents the difference, and it can be sorted into three types depending on the positions in the spectrum, which are d_k^n within the noise spectrum, $d_k^{s\_border}$ existing between adjacent signals, and $d_k^{s\_in}$ existing inside the signals components, respectively.

Then, difference optimization is performed to enable easier filtering. Based on the volatilities of the local minimum groups, we usually consider that $d_k^{s\_in} > d_k^{s\_border} > d_k^n$. Here we need only consider $d_k^{s\_border}$ and d_k^n for division. To enable effective normalization of $\{d_k\}_{k=1}^{m-1}$, the difference detection threshold is set to be

$$\varepsilon_1 = \alpha \times \frac{1}{m-1}\sum_{i=1}^{m-1}d_k \qquad\qquad (13)$$

where α denotes the difference factor that is used to adjust the detection sensitivity. The value of α will be analyzed in the experimental work. The regulatory rule is given by:

$$std_k = \begin{cases} 0 & d_k \le \varepsilon_1 \\ d_k & else \end{cases} \qquad\qquad (14)$$

where std_k denotes the normalized value of d_k. Because of the fluctuations among the different types of differences, most of d_k^n and a small number of $d_k^{s-border}$ are set to zero value; this leads to the partial fluctuations in $d_k^{s-border}$ being reduced or disappearing, while there are almost no fluctuations in the d_k^n; an example for $\alpha = 5$ for a hybrid signal (4FSK+Frank) with $\eta_{s_1} = \eta_{s_2} = 40\%$ is shown in **Fig. 7**.
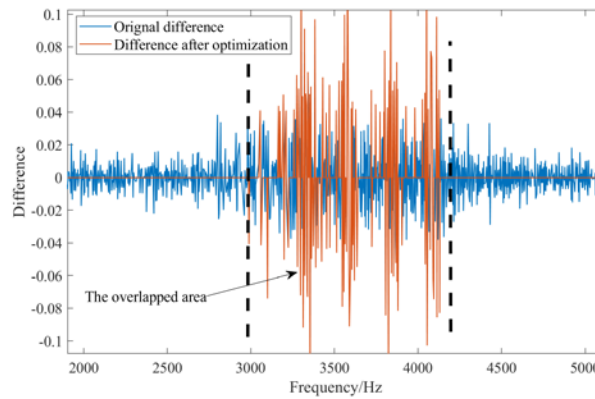

Fig. 7. Comparison between the difference before and after optimization

Finally, the counting and continuity detection of the zero values are performed on the local minimum groups after the difference optimization process. The number of zero values represents the degree of the fluctuations that occur inside the local minimum groups. Larger numbers of zero values correspond to slighter fluctuations, and this regulation can be used to determine whether obvious fluctuations exist within the waveform; this is also the basis used for division. Because energy fluctuations exist between the different frequency bands in MFSK signals, and multiple valley values are generated within the waveforms of MFSK, then these signals can easily be divided into multiple components, which results in destruction of the spectral integrity. In order to address this problem, continuity detection of the zero values works. We define a valid local minimum group with good continuity as a group in which ε_2 zero values are generated, and where most of these zero values are consecutive (the continuity length is set as ε_3 at a minimum), and their could be expressed as follows:

Constraint 3. ε_2 zero values should be within a valid local minimum group that contains K $\min_k$.

Constraint 4. If the number of consecutive zero values in a valid minimum group is larger than ε_3, then the valid group is judged to be with good continuity.

Because the continuity between the different frequency bands of MFSK cannot satisfy these demands, we can then determine that the area of consecutive zero values within a valid local minimum group should be located between adjacent sources or within the noise spectrum, which can be set as an effective boundary area, and the N-1 boundary areas are represented by $\{E_j\}_j^{N-1}$ based on the previous definition. Theoretically, these boundaries can be located anywhere in E_j; here, we define the boundaries ω_i as being at the center of E_j.

4. Results and Analysis

4.1 Setting and Definition of Parameters for Data

Let $\{e_k\}_{k=1}^N$ represent the multiple reconstructed signal components, and then the correlation coefficient ρ for e_k and the source signal s_i is defined as follows:

$$\rho(e_k, s_i) = \frac{1}{Q-1}\sum_{j=1}^{Q}\left(\frac{e_k^j - \mu_{e_k}}{\sigma_{e_k}}\right)\left(\frac{s_i^j - \mu_{s_i}}{\sigma_{s_i}}\right) \tag{15}$$

here, Q represents the length of the sequence e_k, μ_{e_k} and μ_{s_i} are the mean values of e_k and s_i, respectively. σ_{e_k} and σ_{s_i} are the standard deviations of e_k and s_i, respectively.

To obtain a meaningful $\rho(e_k, s_i)$, a threshold ε_3 is used to select the e_k with more information and higher correlation. In general, $\rho(e_k, f) \geq \varepsilon_4$ (usually, $\varepsilon_4 = 0.3$ or 0.4) [23], for filtering, and the set of p reconstructed components is represented by $\{e_j\}_{j=1}^p$. For more comprehensive evaluation of the separation performance, it is necessary to consider the correlations between e_j and all sources $\{s_i\}_{i=1}^n$. We therefore define $segscore_{s_i}$ as the separation coefficient of s_i, which is expressed as follows:

$$sc_i^{\max}\Big|_{j=q} = \max\{|\rho(e_j, s_i)|\}_{j=1}^p \tag{16}$$

$$sc_i^{sum} = \sum_{i=1}^n |\rho(e_q, s_i)| \tag{17}$$

$$\begin{aligned} segscore_{s_i} &= \left|sc_i^{\max} - \left(sc_i^{sum} - sc_i^{\max}\right)\right| \\ &= \left|2sc_i^{\max} - sc_i^{sum}\right| \end{aligned} \tag{18}$$

When $j = q$ ($q \in p$), $|\rho(e_j, s_i)|$ produces the maximum $sc_i^{\max}$, where sc_i^{sum} is the sum of $\{|\rho(e_q, s_i)|\}_{i=1}^{n}$. Larger values of $segscore_{s_i}$ indicate stronger correlation between e_q and s_i, while also corresponding to weaker correlation between e_q and the other sources, and this represents a better separation effect for s_i. Finally, for the input time-frequency overlapped signal f, the overall separation coefficient $segall_f$ is defined as:

$$segall_f = \frac{1}{n} \sum_{i=1}^{n} segscore_{s_i} \tag{19}$$

As the data for experiment, we selected parts of the typical signals and the overlapping conditions from the three time-frequency overlapped signal models for use in testing, and the signal combinations and the related parameters are listed in **Table 1**. The sampling frequency $Fs = 2$ MHz, the random carrier frequency value of each signal is set in the $[1/8, 1/4] \times Fs$ range, and the bandwidth is set in the $[1/16, 1/8] \times Fs$ range. The code length of the Barker signal is 13, and the sequence length of each source is 20000 points.

Table 1. The selected combinations and related parameters in different models

Type	Combination	Number	Bandwidth	Spectrum overlap ratio η (%)
Model 1	EQFM+LFM (EL)	2	EQFM=LFM	[50, 75, 100]
	EQFM+SFM (ES)		EQFM=SFM	
Model 2	EQFM+4FSK(E4F)	2	EQFM>4FSK	4FSK(100)
	LFM+BPSK (LB)		LFM>BPSK	BPSK(100)
Model 3	FRANK+4FSK(F4F)	2	FRANK=4FSK	[20, 40, 60, 80, 100]
	FRANK+Barker(FB)		FRANK=Barker	

In the previous section, the difference detection threshold ε_1 was shown to be highly variable, depending on the difference factor α that was used to adjust the detection sensitivity. Specifically, a larger value of α may generate more sub bands, which would lead to cases where the integrity of an MFSK signal would destroyed more easily. Here, we set ε_2 as 0.5K, and ε_3 as 0.1K, and K represents the number of $\min_k$ in each local minimum group. To select a suitable value of α, **Fig. 8** shows the overall separation coefficient $segall_f$ under various conditions, and we see that when values of α of is equal to 5 or 6, it seems to produce much larger and more stable $segall_f$ values for different input hybrid signals. When α is set smaller, since the obtained number of sub bands is less, then the hybrid signals may still be unsegregated, so the $segall_f$ is smaller.
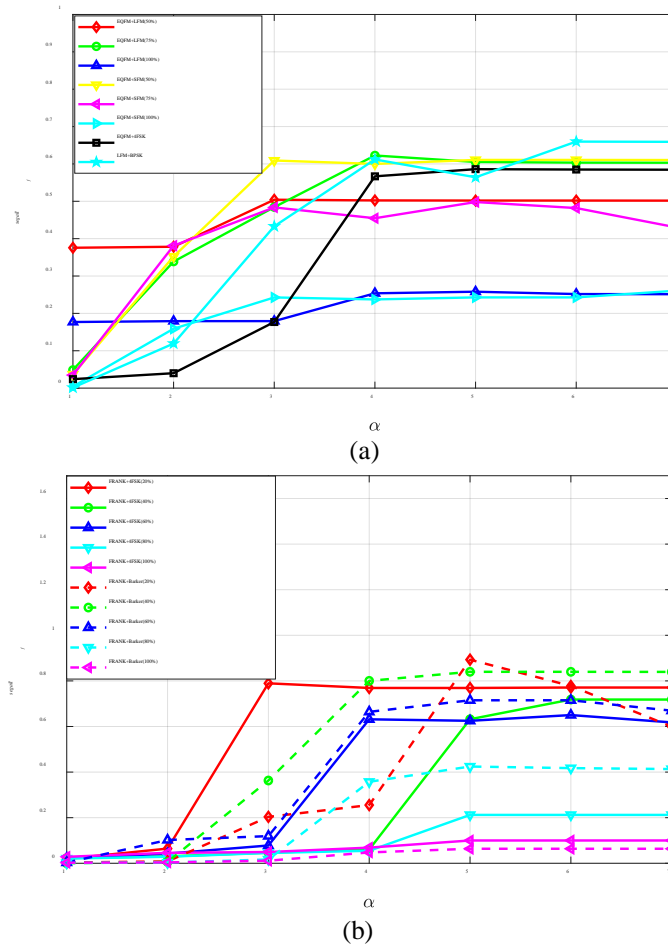
(a)

(b)

Fig. 8. The variation curves of $segall_f$ for different input signal combinations under different values of α . (a) Model 1 and Model 2; (b) Model 3.

4.2 Testing

To compare the classic EWT with the improved EWT in detail, $segscore_{s_i}$ is used to show the separation performance of each source.

For model 1 and model 2, Two different stretch-class distribution signals of the same bandwidth, $[s_1, s_2]$, have an overlap of frequency when $\alpha = 6$; the $segscore_{s_i}$ values are given in **Table 2**. **Table 3** shows the separation performances of the stretch-class distribution component s_3 and the compact-class distribution component s_4 for input, where $\eta_3 = \eta_4 = 100\%$, and $\alpha = 6$.

For model 3, Two compact-class distribution components with the same bandwidth, $[s_5, s_6]$, have an overlap for different spectrum overlap ratios when $\alpha = 5$. The separation performance results are shown in **Table 4**.

When compared with the classic EWT, in the test for model 2, almost all the sources obtained much higher $segscore_{s_i}$ results, thus indicating better separation of the two independent for model 1 and model 3, when $\eta \geq 75\%$, most of the sources gain a slight

improvement when using the improved EWT, although the separation effect is still poor; when $\eta \leq 60\%$, all test signal combinations obtained good and stable separation performances and greatly enhanced $segscore_{s_i}$ results. However, no matter which method is used for the input hybrid signals, if $[segscore_{s_i}, segscore_{s_j}](i \neq j)$ in the same test combination are almost the same, this means that both reconstructed signals will still be in the same sub band, indicating that they have not been separated; this case usually occurs when $\eta \geq 80\%$.

To provide a further overview of the difference between the classic and improved EWTs, we selected the test combinations that have shown good separation performance from the results given above, and calculated the corresponding $segall_f$ for each combination for comparison purposes, with results as shown in **Fig. 9**.

Table 2. The $segscore_{s_i}$ of each source in model 1

(The obvious improved $segscore_{s_i}$ is reported in bold)

Test	$\eta = 50\%$		$\eta = 75\%$		$\eta = 100\%$	
	Classic EWT	**Improved EWT**	**Classic EWT**	**Improved EWT**	**Classic EWT**	**Improved EWT**
EQFM	0.2954	0.3333	0.7218	0.6793	0.2869	0.3020
LFM	0.1896	**0.6707**	0.4218	**0.5665**	0.1237	0.2015
EQFM	0.3521	**0.5220**	0.2108	**0.3458**	0.1648	0.1808
SFM	0.4428	**0.7005**	0.6407	0.6502	0.2680	0.3048

Table 3. The $segscore_{s_i}$ of each source in model 2

(The obvious improved $segscore_{s_i}$ is reported in bold)

| Test	$\eta = 100\%$(4FSK, BPSK)	
	Classic EWT	**Improved EWT**
EQFM	0.5640	**0.6067**
4FSK	0.3421	**0.5652**
LFM	0.2786	**0.6207**
BPSK	0.6981	0.7038

Table 4. The $segscore_{s_i}$ of each source in model 3

(The obvious improved $segscore_{s_i}$ is reported in bold)

Test	$\eta = 20\%$		$\eta = 45\%$		$\eta = 60\%$		$\eta = 80\%$		$\eta = 100\%$	
	Classic EWT	**Improved EWT**	**Classic EWT**	**Improved EWT**	**Classic EWT**	**Improved EWT**	**Classic EWT**	**Improved EWT**	**Classic EWT**	**Improved EWT**
FRANK	0.6015	**0.7921**	0.5630	**0.7833**	0.5664	**0.6671**	0.1401	**0.2790**	0.0773	0.1000
4FSK	0.5265	**0.7497**	0.5051	**0.6530**	0.5546	**0.6781**	0.2701	0.1453	0.0773	0.1000
FRANK	0.7406	**0.8760**	0.7514	**0.8440**	0.7201	0.7536	0.4429	0.4279	0.0273	0.0457
Barker	0.9030	0.9102	0.8636	0.8357	0.7105	0.7038	0.3940	0.4209	0.0273	0.0817
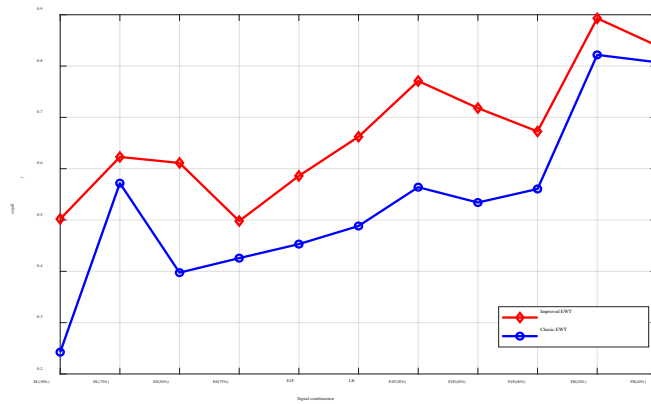
(a)
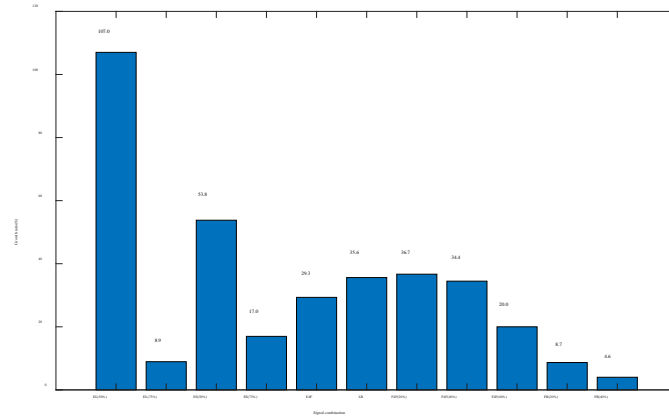
(b)

Fig. 9. (a) The compare of variation curve of $segall_f$ for selected input signal combinations. (b) The compare of the growth rate of the corresponding signal combinations.

The results in **Fig. 9**a show that, in general, for all selected combinations, the separation performance of the improved EWT is always better than that of classic EWT. As for **Fig. 9**b, the growth rate of $segall_f$ is used to quantize the improvements for the different combinations in detail, and the average overall growth rate shows an increase of approximately 32.3%. Among these results, the EQFM+LFM (EL, $\eta = 50\%$) combination shows the highest increase of 107.0%. For the signal combinations containing MFSK, the EQFM+4FSK (E4F) combination increased by 29.3% and the Frank+4FSK (F4F, $\eta = 20\%、40\%、60\%$) showed an average increase of 30.4%. By combining the results given in Table 4 with those of the previous analysis, we find that if $\eta \geq 60\%$, the improved EWT produces very little improvement in the Frank+4FSK (F4F) combination and the separation problem also becomes more difficult.

4.3 Algorithm Complexity

The difference between the classic EWT and the improved EWT mainly lies in the boundary detection approach used, so their algorithm complexities must be analyzed.

The classic EWT determines and filters out the "important maxima" based on a scale-space algorithm, where a Gaussian kernel is used to construct the corresponding low-pass impulse response filter [24]. Because the data in the Fourier spectrum can be regarded as being one-dimensional, the filter is given by:

$$L(n,t) = \sum_{m=-\infty}^{+\infty} f(n-m)g(m;t) \tag{20}$$

where

$$g(m;t) = \frac{1}{\sqrt{2\pi t}} e^{-m^2/2t} \tag{21}$$

Here the filter size is defined as $2m+1$, n is the sequence length of the input one-dimensional Fourier specturm data f , and t is an adjustable scale-space parameter which is finite sequence.

If $n \rightarrow \infty$, then the complexity can be expressed as $T = \mathrm{O}(n^3)$. For the improved EWT, the fast boundary detection mechanism is mainly composed of difference optimization and continuity detection operations. The operations are mostly linear and the quantity of required calculation is relatively small, which is $5n$ at approximately, as shown in **Table 5**.

Table 5. Computational Complexity Comparison of Different Algorithms

Method	Algorithm	Main steps	Complexity
Classic EWT	Scale space algorithm	The construction of discrete spatial scale(Filter construction)	$\mathrm{O}(n^3)$
Improved EWT	Fast boundary detection mechanism	Difference optimization, continuity detection	$\mathrm{O}(n)$

As indicated by the results in **Table 6**, for sample data of the same length and complexity, the operating time of the improved EWT is much shorter than that of the classic EWT, and the average operation speed is increased by approximately 1000 times. As the data length increased, the running time of the improved EWT always maintained a slight increase, thus indicating higher operational efficiency.

Table 6. The Compare of running time (second) between the classic and improved EWT

Data length	Classic EWT	Improved EWT	Ratio(Classic/Improved)
5000	5.0487	0.1218	41
10000	24.4052	0.1352	180
15000	76.7484	0.1573	487
20000	175.4452	0.1593	1101
25000	401.1256	0.2206	1818
30000	705.7267	0.2558	2759

5. Conclusion

Through the introduction of a fast boundary detection mechanism, this paper proposes an effective method for separation of single-channel time-frequency overlapped radar and

communication signals based on an improved empirical wavelet transform (EWT). To optimize the sub-band division approach, difference optimization and continuity detection techniques were used to replace the scale-space algorithm used in the classic EWT. The improved EWT improves the separation performance of input hybrid signals, specifically maintaining the integrity of MFSK signals during division, while also achieving good processing efficiency. At spectrum overlap ratios of less than 60%, the improved EWT provides a much better performance than the classic EWT. However, when the spectrum overlap ratio is more than 60%, the improved EWT cannot be used to implement separation in a similar manner to the classic EWT.

References

[1] Guo Q, Li C, Ruan G, "Mixing Matrix Estimation of Underdetermined Blind Source Separation Based on Data Field and Improved FCM Clustering," *Symmetry*, vol. 10, no. 1, 21, January 2018. Article (CrossRef Link).

[2] Ge X, Sun Y, Gharavi H, et al., "Joint Optimization of Computation and Communication Power in Multi-user Massive MIMO Systems," *IEEE Transactions on Wireless Communications*, vol. 17, no. 6, pp. 4051-4063, June 2018. Article (CrossRef Link).

[3] Virta J, Nordhausen K, "Blind source separation of tensor-valued time series," *Signal Processing*, vol. 141, pp. 204-216, December 2017. Article (CrossRef Link).

[4] Peng T, Yang C, "A Time-Frequency domain blind source separation method for underdetermined instantaneous mixtures," *Circuits Systems & Signal Processing*, vol. 34, no. 12, pp. 3883-3895, March 2015. Article (CrossRef Link).

[5] Jiménezgonzález A, James C J, "Extracting sources from noisy abdominal phonograms: a single-channel blind source separation method," *Medical & Biological Engineering & Computing*, vol. 47, no. 6, pp. 655-664, March 2009. Article (CrossRef Link).

[6] Yongjian Liu, Peng Xiao, Hongchao Wu, Weihua Xiao, "LPI radar signal detection based on radial integration of Choi-Williams time-frequency image," *Journal of Systems Engineering and Electronics*, vol. 26, no. 5, pp. 973-981, December 2015. Article (CrossRef Link).

[7] Z Jing M, Mcginnity T M, Coleman S, et al., "Enhancement of Fiber Orientation Distribution Reconstruction in Diffusion-Weighted Imaging by Single Channel Blind Source Separation," *IEEE Transactions on Biomedical Engineering*, vol. 59, no. 2, pp. 363-373, October 2012. Article (CrossRef Link).

[8] Zhang Xing, "Research on detection, recognition and separation technologies for the multi-carrier mixed signal," *University of Electronic Science and technology of China*, 2017. Article (CrossRef Link).

[9] Zhao Yufeng, "Single channel blind separation of time-frequency overlapped communication signals," *University of Science and Technology of China*, 2015. Article (CrossRef Link).

[10] Zhang Y, Zhang S, Qi R, "Compressed Sensing Construction for Underdetermined Source Separation," *Circuits Systems & Signal Processing*, vol. 36, no. 11, pp. 4741-4755, November 2017. Article (CrossRef Link).

[11] Vipin K. Mishra, Varun Bajaj, Anil Kumar, Dheeraj Sharma, G.K. Singh, "An efficient method for analysis of EMG signals using improved empirical mode decomposition," *AEU - International Journal of Electronics and Communications*, vol. 72, pp. 200-209, February 2017. Article (CrossRef Link).

[12] Pang Lihui, "Research on signal separation method for time-frequency overlapped digital communication signal from single antenna," *University of Electronic Science and technology of China*, 2015. Article (CrossRef Link).

[13] Cheng Xiefeng, Ma Yong, Zhang Xuejun, et al., "A single-channel mixed signal bss new method without using the prior knowledge," *ACTEA ELECTRONICA SINICA*, vol.39, no. 10, pp. 2317-2321, October 2011. Article (CrossRef Link).

[14] Venkatappareddy P, Lall B, "Characterizing Empirical Mode Decomposition Algorithm Using Signal Processing Techniques," *Circuits Systems & Signal Processing*, vol. 37, no. 7, pp. 2969-2996, November 2018. Article (CrossRef Link).

[15] Yang Yanli, Deng Jiahao, "Analysis on frequency resolution of EMD based on B-spline interpolation," *AEU - International Journal of Electronics and Communications*, vol. 70, no. 9, pp. 1235-1240, September 2016. Article (CrossRef Link).

[16] Li Y, Chen X, et al., "Research on Ship-Radiated Noise Denoising Using Secondary Variational Mode Decomposition and Correlation Coefficient," *Sensors*, vol. 18, no. 1, 48, December 2018. Article (CrossRef Link).

[17] Kedadouche M, Thomas M, Tahan A, "A comparative study between Empirical Wavelet Transforms and Empirical Mode Decomposition Methods: Application to bearing defect diagnosis," *Mechanical Systems & Signal Processing*, vol. 81, no. 15, pp. 88-107, December 2016. Article (CrossRef Link).

[18] Gilles J, "Empirical Wavelet Transform," *IEEE Transactions on Signal Processing*, vol. 61, no. 16, pp. 3999-4010, May 2013. Article (CrossRef Link).

[19] Thirumala K, Shantanu, Jain T, et al., "Visualizing time-varying power quality indices using generalized empirical wavelet transform," *Electric Power Systems Research*, vol. 143, pp. 99-109, February 2017. Article (CrossRef Link).

[20] Feng Z, Liang M, Chu F, "Recent advances in time–frequency analysis methods for machinery fault diagnosis: A review with application examples," *Mechanical Systems & Signal Processing*, vol. 38, no. 1, pp. 165-205, July 2013. Article (CrossRef Link).

[21] Zhang M, Liu L, Diao M, et al., "LPI Radar Waveform Recognition Based on Time-Frequency Distribution," *Sensors*, vol. 16, no. 10, 1682, October 2016. Article (CrossRef Link).

[22] Daubechies I, "Ten Lectures on Wavelets" *CBMS-NSF Regional Conference Series in Applied Mathematics, The Society for Industrial and Applied Mathematics: Philadelphia, PA, USA*, 1992. Article (CrossRef Link).

[23] Zhao Miaoying, Xugang, "Feature Extraction for Vibration Signals of Power Transformer Based on Empirical Wavelet Transform," *Automation of Electronic Power Systems*, vol. 41, no. 20, pp. 63-69, October 2017. Article (CrossRef Link).

[24] Gilles J, Kathryn Heal, "A parameterless scale-space approach to find meaningful modes in histograms u2014 Application to image and spectrum segmentation," *International Journal of Wavelets Multi resolution & Information Processing*, vol. 12, no. 6, 1450044, 2014, 12(06):1450044. Article (CrossRef Link).

Liu Zhipeng received his B.S degree in Electronic Information Engineering (2012) from Information Engineering University in Zhengzhou. He is now a master student of National Digital System Engineering and Technological Research Center, Zhengzhou. His research areas focus on: blind source separation, machine learning and application.
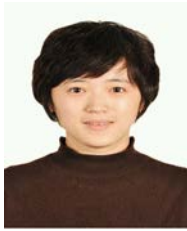
Li Lichun now is an Associate Professor in National Digital System Engineering and Technological Research Center. Her main research interests include compressed sensing, communicational signal processing, blind source separation, complex hybrid signals processing and recognition and machine learning.

Li Huiqi received his M.S degree (2018) in Information Engineering (2012) from Information Engineering University in Zhengzhou. His research areas focus on: gridless compressed sensing and frequency-hopping signal detection.

LiuChang received the B.S degree in Environmental Science (2016) from Nanchang University. He is now a master student of School of Environmental Science and Engineering, Nanchang University. His research areas focus on: signal processing, the interaction between surface water and groundwater， using groundwater modeling software to simulate groundwater flow.